Boundary homogenization and numerical modeling of solute transport across the blood-brain barrier

Reza Yousofvand [1], Gregory Handy [2,*,†] and Jeffrey Tithof [1,*,‡]
[1]*Department of Mechanical Engineering, University of Minnesota, Minneapolis, Minnesota 55455, USA*
[2]*School of Mathematics, University of Minnesota, Minneapolis, Minnesota 55455, USA*

(Received 1 July 2025; accepted 30 October 2025; published 21 November 2025)

Effective clearance of amyloid-β (Aβ) from the brain is essential for preventing neurodegenerative diseases such as Alzheimer's. A significant portion of this clearance occurs through the blood-brain barrier (BBB) via receptor-mediated transport. However, current models fail to capture the complex kinetics and spatial heterogeneity of receptors at the BBB. In this study, we derive a boundary condition that accounts for finite receptor kinetics, receptor density, and bidirectional transport across the BBB. Specifically, we develop a nonlinear homogenized boundary condition that ensures mass conservation and incorporates receptor-mediated Michaelis-Menten kinetics. We then implement this boundary condition in a cylindrical geometry representing a capillary surrounded by brain tissue. After verifying that the model matches an analytical steady-state solution that we derive and that it yields realistic blood Aβ concentrations, we explore how realistic variations in parameter values drive changes in both steady-state Aβ concentration and transient dynamics. Simulations and analytical results reveal that Aβ concentrations in the brain are sensitive to receptor number ratios, while concentrations in the blood are primarily affected by the blood clearance rate. Additionally, we use the model to investigate Aβ clearance during sequential sleep cycles and due to a pathological phenomenon, spreading depolarization. This work presents a biophysically consistent boundary condition for Aβ transport across the BBB, offering a powerful tool for studying brain waste clearance under both physiological and pathological conditions.

DOI: 10.1103/qr7v-btpp

I. INTRODUCTION

An inevitable outcome of cellular metabolism is the generation of waste products. In most tissues, interstitial fluid containing these cellular by-products drains into lymphatic vessels, which transport the fluid to the venous bloodstream. From there, the waste is distributed to various organs and eventually cleared from the body. However, the lymphatic system is absent in the brain. Being a highly active organ, the brain produces waste proteins such as amyloid-β (Aβ) that require clearance. If not cleared effectively, Aβ accumulates in the brain and results in development of diseases such as Alzheimer's and related dementias [1–3]. Other than metabolic degradation, Aβ is cleared through the blood-brain barrier (BBB) to be carried away via blood flow or through the glymphatic system. The glymphatic system is a brain-wide clearance pathway in which cerebrospinal fluid (CSF) flows through perivascular spaces (PVSs) surrounding penetrating vessels, facilitating waste removal from the brain via regulated transport across astrocyte endfeet [4–9].

In humans, 50% of all generated Aβ in the brain is eliminated by proteolytic degradation, and from the remaining 50%, approximately half is cleared through CSF flow, and the other half is cleared through the BBB [5]. Similarly, in mice, about 27% of total Aβ clearance is mediated by the BBB [10]. A higher contribution of BBB in clearance has been reported using the brain efflux index method, which indicated that 62% of intracerebrally injected Aβ appeared in the blood [11]. These measurements illustrate the significance of the BBB in clearing Aβ from the brain and thus highlight its role in preventing the development of neurodegenerative diseases related to Aβ accumulation.

The BBB is a highly selective semipermeable border of endothelial cells around blood vessels that tightly regulates the movement of ions, molecules, and cells between the blood and the brain. For Aβ, two so-called "active transporters" exist, the receptor for advanced glycation end products (RAGE) and low-density lipoprotein receptor related protein-1 (LRP1) [12,13]. LRP1, expressed on the abluminal side of brain endothelial cells, facilitates the efflux of Aβ from the brain into the cardiovascular circulation. This receptor-mediated transport is essential for reducing Aβ accumulation in the brain parenchyma [14–16]. Conversely, RAGE, located on the luminal side of endothelial cells, mediates the influx of circulating Aβ into the brain [17–19]. The balance between LRP1-mediated efflux and RAGE-mediated influx is therefore crucial in regulating brain Aβ levels [20]. A mathematical representation of the BBB that captures the physical behavior of the receptor-based boundary is essential for reliable simulation of Aβ clearance from the brain. Currently, no available mathematical model in the literature accounts for

*These authors contributed equally to this work.
†Contact author: ghandy@umn.edu
‡Contact author: tithof@umn.edu

the size, number, and kinetics of receptors on both sides of the BBB.

A foundational framework for modeling receptor-mediated diffusion processes was laid by Berg and Purcell [21], who developed a theory for the accuracy of chemoreception in biological systems by considering the diffusive flux of particles to a spherical surface sparsely decorated with receptors. They demonstrated that the flux of ligands to receptors scales linearly with both the receptor size and number, and they introduced the concept of a "diffusive limit" for sensing, which remains central in quantitative models of cell signaling. This classical model was extended by introducing time-dependent treatments of ligand binding to spheres partially covered by receptors [22]. This model showed that the early-time binding kinetics differ significantly from steady-state assumptions and that the total flux approaches the Berg-Purcell prediction only after a transient phase. A central aspect of many receptor-based models is the incorporation of Michaelis-Menten kinetics, originally developed to describe enzyme-catalyzed reactions [23]. This kinetic framework assumes that the reaction rate is proportional to the concentration of the ligand and saturates as receptor sites become occupied. In the context of diffusive transport and boundary models, the Michaelis-Menten formalism appears as a nonlinear Robin boundary condition that captures saturable binding at the surface. Specifically, the flux into the boundary is modeled as $D\frac{\partial C}{\partial n} = \frac{k_{\text{on}} N_{\text{tot}} C}{K_m + C}$, where C is the concentration, n is the normal vector to the surface, k_{on} is the binding rate constant, N_{tot} is the total receptor density, and K_m is the Michaelis constant. This form was explored by considering dynamic traps that switch between active and inactive states, effectively implementing a time-dependent MichaelisMenten-type behavior at the boundary [24].

Further refinements involved homogenization techniques where a patchy absorbing surface could be approximated using a Robin boundary condition—an approach which replaces a mixed Dirichlet-Neumann boundary with an effective single boundary of the form $D\frac{\partial C}{\partial n} = \kappa C$, where κ encodes partial absorption [25,26]. This effective medium theory simplifies modeling of surfaces with distributed receptors without resolving each patch individually. It has been formalized for narrow-escape and mean first-passage time problems on spherical targets with small absorbing patches [27], and extended to planar surfaces with periodic patches [28]. Further developments incorporate anisotropic diffusion and rotational effects for patchy particles [29]. More recently, the classical Berg-Purcell model was revised by including finite receptor kinetics, showing that traditional models can greatly overestimate uptake rates [30].

In this current study, we extend the receptor-mediated diffusion model with finite receptor kinetics [30] to develop a boundary condition for the BBB. To achieve this, we update the previous model to account for two domains—brain and blood—with the BBB at their interface. This BBB boundary model incorporates the number, size, and kinetics of BBB receptors. We couple this boundary condition with a diffusion model for Aβ transport through the brain. Aβ monomers pass between the two domains via receptors on each side, while maintaining mass conservation. First, we derive the boundary condition using brain-specific and Aβ-specific assumptions.

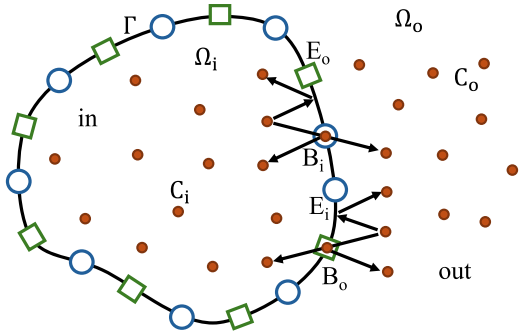

FIG. 1. Schematic of solute transport between two domains via binding receptors. The two "in" and "out" domains are separated by the surface Γ, and the inner (C_i), and outer (C_o) substrates can be transported across the boundary between the domains. E_α and B_α represent the enzyme and bound complex for the inner and outer receptors, respectively.

Then we solve the steady-state diffusion problem analytically using the derived boundary condition. We next solve the problem numerically to analyze BBB behavior in brain waste clearance; we both verify our numerical method against analytical results and validate the predicted Aβ concentrations against measurements reported in the literature. We highlight the sensitive dependence of Aβ on a few key parameters which are known to vary with aging.

Finally, we adapt our numerical simulations to investigate transient Aβ changes in one complex physiological and one complex pathological scenario. Sleep has been linked to decrease in Aβ concentration in the brain [31], and growing evidence suggests sleep disruption contributes to Alzheimer's pathology [32,33]. We perform sleep simulations that indicate rapid eye movement (REM) sleep may play a vital role in Aβ clearance. The complex pathological scenario we consider is spreading depolarization (SD), which is a wave of abnormal neuronal activity that propagates through the cerebral cortex and occurs due to a loss of brain ion homeostasis [34]. Spreading depolarization is associated with migraine with aura (as well as many other neurological disorders) [35], and migraine is linked to an increased risk of dementia [36,37]. We perform simulations that predict transient changes in Aβ concentration due to SD which may help explain such associations. Because both sleep and SD are inherently time-dependent processes, we modeled them using transient simulations. By varying blood flow rate and capillary size over different time stages, we captured these scenarios. The corresponding results are presented in the transient part of the results section.

II. METHODS

A. Boundary homogenization

We start by creating a general receptor-mediated diffusion problem involving two domains, as illustrated in Fig. 1. In this model, diffusing substrates (with concentration $C_\alpha, \alpha = \{i, o\}$) can pass through the distributed transporters on the boundary Γ separating the inner (Ω_i) and outer (Ω_o) domains. These substrates can bind to enzymes (E_α) on the walls, which act as transporters, allowing the substrates to travel between the two domains. During this process, a substrate that binds to an

enzyme forms a bound complex (B_α). The enzymes responsible for transporting substrates from the outer to the inner domain may differ from those facilitating transport from the inner to the outer domain. Once a bound complex is formed, the substrate can either be transported across the domain or released back into its starting domain. Additionally, a bound complex can transport only one substrate at a time.

The advection-diffusion equations for the inner and outer domains (indicated with subscripts i and o, respectively) can be written as

$$\frac{\partial C_i}{\partial t} = D_i \nabla^2 C_i - \vec{u}_i \cdot \vec{\nabla} C_i + G_i(C_i), \vec{x} \in \Omega_i, \tag{1}$$

$$\frac{\partial C_o}{\partial t} = D_o \nabla^2 C_o - \vec{u}_o \cdot \vec{\nabla} C_o + G_o(C_o), \vec{x} \in \Omega_o, \tag{2}$$

where C_α is a scalar field representing the concentration of the substrate, D_α is the substrate's diffusivity, $\vec{u}_\alpha$ represents the velocity field, and G_α accounts for substrate generation within the domain. To solve the system of Eqs. (1) and (2), we require a boundary condition for the wall that separates the domains, which is defined as

$$D\frac{\partial C_i(\Gamma)}{\partial n} = \kappa_{rec} C_i, \quad \text{In a receptor,} \tag{3}$$

$$D\frac{\partial C_o(\Gamma)}{\partial n} = 0, \quad \text{Not in a receptor.} \tag{4}$$

To homogenize the boundary condition in Eq. (3) we replace it with a homogeneous boundary condition as

$$D\frac{\partial C_i}{\partial r} = \kappa C_i, \; r = R, \tag{5}$$

where trapping rate κ is chosen to incorporate the number, size, and arrangement of receptors for the specific system. We apply the classical substrate and enzyme reaction scheme at the boundary for both domains, as follows [38]:

$$C_i + E_i \underset{k_i^b}{\overset{k_i^a}{\rightleftharpoons}} B_i \overset{k_i^c}{\rightarrow} C_o + E_i \tag{6}$$

$$C_o + E_o \underset{k_o^b}{\overset{k_o^a}{\rightleftharpoons}} B_o \overset{k_o^c}{\rightarrow} C_i + E_o \tag{7}$$

where k^a, k^b, and k^c represent the rates of association, breakup, and catalysis, respectively. Initially we assume that these rates are different for receptors associated with each direction. Additionally, since the receptors for each direction are different, the enzyme E_α and the bound complex B_α are not equal. Using chemical equations (6) and (7) and the law of mass action, we can formulate a homogeneous boundary condition for the flux exiting the inner domain as

$$D_i \frac{\partial C_i(\Gamma, t)}{\partial n} = -k_i^a e_i(t) C_i(\Gamma, t) + b_i(t) k_i^b + b_o(t) k_o^c, \tag{8}$$

where $e_i(t)$ and $b_i(t)$ are free receptor and bound receptor concentrations, respectively, and satisfy the following equations:

$$\frac{de_i(t)}{dt} = -k_i^a e_i(t) C_i(\Gamma, t) + b_i(t)\left(k_i^b + k_i^c\right), \tag{9}$$

$$\frac{db_i(t)}{dt} = k_i^a e_i(t) C_i(\Gamma, t) - b_i(t)\left(k_i^b + k_i^c\right), \tag{10}$$

which satisfies the total receptor concentration. From Eqs. (9) and (10), one can obtain the conservation equation $e_i(t) = e_{0,i} - b_i(t)$, where $e_{0,i}$ represents the number of receptors per unit surface area. Consequently, we can eliminate $e_i(t)$ from Eqs. (8) and (10), rewriting them as

$$D_i \frac{\partial C_i(\Gamma, t)}{\partial n} = k_i^a (b_i(t) - e_{0,i}) C_i(\Gamma, t) + b_i(t) k_i^b + b_o(t) k_o^c, \tag{11}$$

$$\frac{db_i(t)}{dt} = k_i^a [e_{0,i} - b_i(t)] C_i(\Gamma, t) - b_i(t)\left(k_i^b + k_i^c\right). \tag{12}$$

In cases where the volume concentrations of receptors are considerably smaller than those of the substrates, Briggs and Haldane's derivation adopts the steady-state approximation [39]. This approximation is based on the observation that in most systems (including the BBB system that is the focus of this work), the concentration of the bound complex will quickly reach a steady state after an initial burst phase, then its concentration will remain relatively stable until a significant amount of substrate has been consumed. Therefore, we can rewrite Eq. (12) using the steady-state approximation ($db/dt = 0$) as

$$0 = e_{0,i} k_i^a C_i(\Gamma, t) - b_i(t)\left[k_i^b + k_i^c + k_i^a C_i(\Gamma, t)\right], \tag{13}$$

which leads to

$$b_i(t) = \frac{e_{0,i} k_i^a C_i(\Gamma, t)}{k_i^b + k_i^c + k_i^a C_i(\Gamma, t)}. \tag{14}$$

By substituting this expression into Eq. (11), we have

$$D_i \frac{\partial C_i(\Gamma, t)}{\partial n} = -\frac{V_i C_i(\Gamma, t)}{K_i + C_i(\Gamma, t)} + \frac{V_o C_o(\Gamma, t)}{K_o + C_o(\Gamma, t)}, \tag{15}$$

where the maximal reaction velocity and half-saturation constant for each domain are defined as

$$V_i = e_{0,i} k_i^c, \quad K_i = \frac{k_i^b + k_i^c}{k_i^a},$$

$$V_o = e_{0,o} k_o^c, \quad K_o = \frac{k_o^b + k_o^c}{k_o^a}. \tag{16}$$

Following the same steps for the flux entering the outer domain yields the same flux but with a different sign, ensuring mass conservation:

$$D_o \frac{\partial C_o(\Gamma, t)}{\partial n} = -D_i \frac{\partial C_i(\Gamma, t)}{\partial n}. \tag{17}$$

This completes the derivation of the boundary condition for the membrane separating the two domains in the problem introduced in Eqs. (1) and (2).

B. Aβ transport across the BBB

As previously discussed, Aβ clearance across the BBB plays a crucial role in maintaining brain homeostasis through transporter-mediated mechanisms [3,5,10,12,13]. We adapt the introduced boundary condition to simulate Aβ transport through the BBB. The domain consists of two concentric cylinders, where the inner cylinder represents the capillary, and the outer cylinder represents the surrounding brain tissue. Figure 2 illustrates the concentration distribution for a capillary surrounded by brain tissue, where transport occurs. Equations (1) and (2) can be modified to capture this transport by considering waste removal in the vessel due to blood

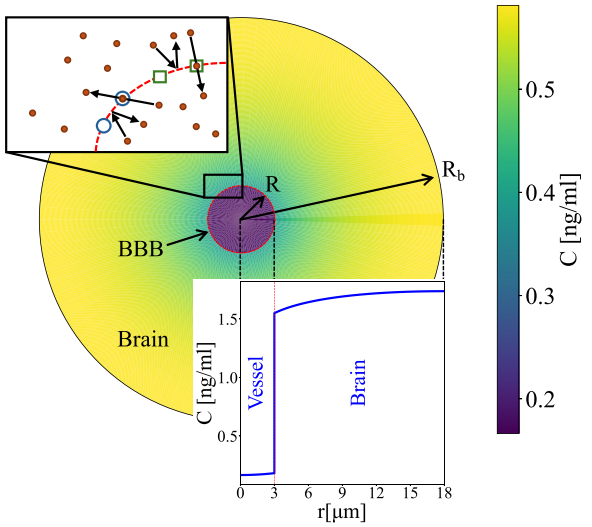

FIG. 2. Schematic diagram of the axisymmetric simulation domain. The color contour indicates the Aβ concentration C. The one-dimensional plot (bottom) quantifies the concentration profile as a function of radius r. The zoomed view of the boundary (top left) illustrates the BBB receptor kinetics that we model.

advection (inner domain) and the natural generation of Aβ in the brain (outer domain). The modified equations, under the assumption of axisymmetry, are as follows:

$$\frac{\partial C_i(r,t)}{\partial t} = D_i\left[\frac{1}{r}\frac{\partial}{\partial r}\left(r\frac{\partial C_i(r,t)}{\partial r}\right)\right] - \beta C_i(r,t), \tag{18}$$

$$\frac{\partial C_o(r,t)}{\partial t} = D_o\left[\frac{1}{r}\frac{\partial}{\partial r}\left(r\frac{\partial C_o(r,t)}{\partial r}\right)\right] + G, \tag{19}$$

where β is blood sink coefficients, a constant accounting for Aβ clearance in the blood due to advection, and G is the production of Aβ that occurs naturally in the brain. Beyond the shared boundary conditions at the BBB, one additional boundary condition is required for each domain. The following boundary conditions are assumed for the inner and outer domains due to the symmetry of the geometry:

$$\frac{\partial C_i}{\partial r} = 0,\ r = 0, \tag{20}$$

$$\frac{\partial C_o}{\partial r} = 0, r = R_b. \tag{21}$$

The boundary condition introduced in Eq. (15) is adjusted to represent Aβ transport between the two domains. We assume $k^b = 0$ in Eqs. (6) and (7), meaning that when Aβ monomers bind to the BBB receptors, they are transferred to the other side without dissociation. The trapping rate κ in Eq. (5) is defined as

$$\kappa = \frac{\sigma\kappa_{\rm rec}\bar{\kappa}_{BP}}{\sigma\kappa_{\rm rec} + \bar{\kappa}_{BP}}. \tag{22}$$

In this expression $\kappa_{\rm rec}$ is the rate that a receptor binds a substrate. Additionally, surface trapping rate $\bar{\kappa}_{BP}$ and receptor area fraction σ are defined as

$$\bar{\kappa}_{BP} = \frac{4\pi\sigma}{\pi a},\ \sigma = \frac{N\pi a^2}{2\pi RL}, \tag{23}$$

where a and N represent the receptor radius and the number of receptors, respectively, and L is the unit length along the axis of the capillary. By choosing ϵ as the ratio of the receptor radius to the vessel radius and substituting Eq. (23) into Eq. (22), we obtain

$$\kappa = \frac{2DN\epsilon}{\pi L}\left(1 + \frac{4D}{\pi\epsilon R\kappa_{\rm rec}}\right)^{-1}. \tag{24}$$

Following the Berg and Purcell approximation, in which a receptor absorbs the substrate immediately upon contact, we consider $\kappa_{\rm rec} \to \infty$ [21,30]. In this limit, κ can be substituted into Eq. (5). Furthermore, assuming that all receptors are free, i.e., $b(t) = 0$, Eq. (11) simplifies to Eq. (5).Therefore, assuming a similar radius for the receptors that transfer Aβ from brain to blood as for those that transfer from blood to brain ($\epsilon_i = \epsilon_o$), and assuming a small thickness of the vessel wall, the rate of association for the blood and brain sides becomes

$$k^a_\alpha = 4D_\alpha\epsilon R, \tag{25}$$

where $\alpha = \{i, o\}$. The receptor concentration per unit surface area, e_0, for a cylindrical vessel can be calculated as

$$e_{0,\alpha} = \frac{N_\alpha}{2\pi RL}. \tag{26}$$

Additionally, we assume that the rate of catalysis (k^c) is the same for both the blood and brain sides. Applying these assumptions to Eq. (16), Eq. (15) can be rewritten as follows:

$$D_i\frac{\partial C_i(R,t)}{\partial r} = -\frac{N_i k^c}{2\pi RL}\frac{C_i(R,t)}{\frac{k^c}{k^a_i} + C_i(R,t)} + \frac{N_o k^c}{2\pi RL}\frac{C_o(R,t)}{\frac{k^c}{k^a_o} + C_o(R,t)}. \tag{27}$$

The nondimensional form of this boundary condition, as well as the governing equations (18)–(19), are available in Sec. I of the Supplemental Material [40]. The complexity of this boundary condition arises from the fact that it accounts for the number, size, and kinetics of the BBB receptors, as well as the saturation of transport due to high concentrations at the boundary. Since this study focuses on Aβ transport, the assumptions are formulated based on the transfer dynamics of this protein between blood and brain. These assumptions can also be extended to other transport processes across the BBB and are summarized as follows:

(1) Distinct receptors mediate transport in each direction (E_i and E_o).

(2) Once monomers bind to receptors, they are transferred to the opposite side ($k_b = 0$).

(3) Receptor sizes are identical on both sides ($\epsilon_i = \epsilon_o$).

(4) The diffusion coefficients differ across the two sides ($D_i \neq D_o \Rightarrow k^a_i \neq k^a_o$).

(5) Receptor concentrations differ across the two sides ($N_i \neq N_o$).

(6) Mass conservation is satisfied: any monomer leaving one domain enters the other.

To assess the significance of these complexities, we performed simulations using a simplified linear form of the boundary condition and observed a significant difference compared to the results obtained with the complete version. This comparison is provided in Sec. II of the Supplemental Material [40].

TABLE I. Parameters used in simulations.

Parameter	Definition	Range	Default value	Reference
N_i/L	Number of LRP1 receptors	$[2\times10^3, 2\times10^4]$ no./μm	2×10^4 no./μm	Kyrtsos *et al.* [44]
N_o/L	Number of RAGE receptors	$[2\times10^3, 2\times10^4]$ no./μm	2×10^4 no./μm	—
a	Receptor radius		10^{-3} μm	—
β	Blood sink coefficient	$[1, 10^3]$ s^{-1}	10 s^{-1}	—
k_c	Turnover rates of transporter	$[1, \infty]$ s^{-1}	10 s^{-1}	—
R	Capillary radius	[2.5, 4] μm	3 μm	Miyawaki *et al.* [45]
R_b	Half the capillary-capillary distance		18 μm	[42,43]
D	Aβ diffusivity		230 $\mu m^2/s$	Sykova *et al.* [41]
λ	Tortuosity of brain		2.04	Sykova *et al.* [41]
G	Aβ production		0.1 ng/(ml s)	Yousofvand *et al.* [42]

C. Numerical method

As mentioned, we consider an averaged cross-sectional domain consisting of a capillary and its corresponding surrounding portion of brain tissue (Fig. 2). In this configuration, variations in axial direction are averaged, and the problem exhibits azimuthal symmetry. Therefore, the model is reduced to an axisymmetric one-dimensional (1D) cylindrical problem with variations in the r direction, referenced from the center of the capillary. To solve the problem with the introduced boundary conditions, we developed a numerical model using the finite difference method. We employed an explicit time integration scheme with the forward Euler method, which is second-order accurate in space (based on central finite differences) and first-order accurate in time. The implementation details of the boundary condition in Eq. (27) are provided in Sec. III of the Supplemental Material [40].

First, we nondimensionalized the equations and boundary conditions and simulated the problem for both transient and steady-state cases (see Sec. I in the Supplemental Material [40]). The vessel and brain domains are simulated within separate computational domains, and the interface boundary condition is handled by applying the flux introduced in Eq. (27) at the right boundary of the vessel domain and the left boundary of the brain domain. To ensure steady state, a criterion of $(C^n_{\max} - C^{n-1}_{\max})/C^{n-1}_{\max} < 10^{-10}$ is enforced, where n represents the iteration number and $C_{\max}$ is the highest concentration in the domain. Figure 2 shows a contour and a profile of concentration distribution in the vessel and brain.

D. Parameter range

To perform simulations, we need to specify the parameters used in the equations. Since determining some biological values requires challenging *in vivo* experimental measurements we focus on the mouse brain where more data are available, and as these measurements are prone to substantial biological variability and large uncertainties, we test a range of these parameters. The radius of capillaries ranges from 2.5 μm, approximately the size of a red blood cell, to 4 μm. Additionally, as mentioned, LRP1 is primarily responsible for mediating the efflux of Aβ from the brain interstitial fluid into the blood and RAGE is involved in transporting circulating Aβ from the blood into the brain. In Eq. (27), we specify the number of these receptors per unit length (N/L), and the N_o/N_i ratio determines the weight of transport in each direction.

The diffusivity of Aβ in a free medium is $D = 2.3\times10^{-10}$ m^2/s [41]. This value is used for Aβ diffusion in the blood ($D_i = D$). To account for the porous nature of brain tissue, the diffusivity of Aβ is modified by the tortuosity of the brain tissue, $D_o = D_{\text{eff}} = D/\lambda^2$ where $\lambda = 2.04$ [41]. Additionally, the size of the domain (R_b) is defined as half of the average distance between capillaries in mice brain, which is calculated to be approximately 36 μm [42]. The spacing yields a mean distance of 11 μm from any extravascular point to the nearest capillary wall, verified computationally and chosen based on the peak of the probability distribution obtained from mouse experiments [43]. A list of parameter ranges used for the simulation is provided in Table I. A column of default values is provided in the table, and unless otherwise stated in the figure captions, all results use these default values.

The introduced LRP1 receptor number is used as the default value for both LRP1 (N_o/L) and RAGE (N_i/L), and variations in N_o/N_i relative to this default value are analyzed. Although a range of capillary sizes is considered, a default size of 3 μm is used for simulations. Additionally, since half of the generated Aβ monomers are removed by the BBB, we consider half of the production rate provided in Table I for the source term G in Eq. (19) (i.e., we exclude the half of production that would be cleared via CSF).

III. RESULTS

A. Steady-state results

After creating the domain and defining the boundary conditions, we perform simulations for various cases. We begin with steady-state analysis of the concentration profile in the domain for different blood sink coefficients (β) and receptor number ratios (N_o/N_i). Figure 3(a) illustrates the concentration profile for different receptor number ratios with $\beta = 10\,s^{-1}$. The saturation level is highly dependent on the receptor number ratio, with higher saturation concentration observed on the side of the boundary with fewer receptors. Interestingly, we find that the concentration profile inside the vessel is independent of receptor number ratios and depends only on β. From the analytical solution for the steady-state concentration inside the vessel, provided in Sec. IV of the Supplemental Material [40], we observe that the concentration in the vessel is in fact independent of the receptor number ratio, which verifies our numerical model.

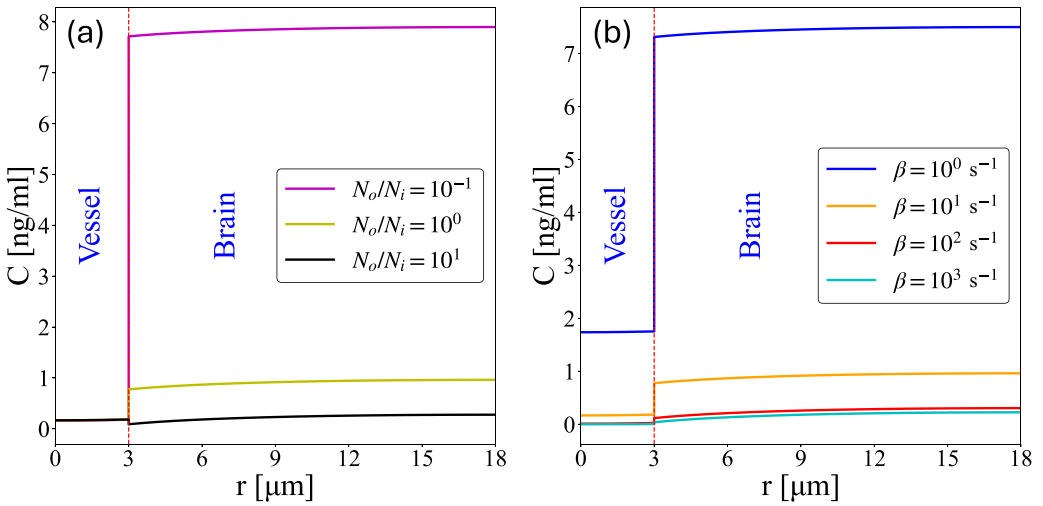

FIG. 3. Steady-state concentration profiles for (a) different N_o/N_i with $\beta = 10\,\mathrm{s}^{-1}$ and (b) different β values with $N_o/N_i = 1$.

An important observation in Fig. 3 is the concentration level of Aβ calculated in the vessel. It has been shown that the concentration of Aβ in plasma in the mouse brain is approximately 0.1–0.2 ng/ml [46]. A similar concentration level is observed in our simulations for $\beta = 10\,\mathrm{s}^{-1}$. This agreement is achieved using the boundary condition from Eq. (27), along with the receptor numbers and the production rate of Aβ specific to the mouse brain, thereby validating our model. To better interpret these results, we examine the role of β in the model. Comparing Eq. (18) with the advection-diffusion equation in a vessel shows that the term $\beta C_i(r,t)$ is analogous to the advection term $u\frac{\partial C}{\partial z}$, where u is the velocity along the vessel axis z. For a capillary of characteristic axial length L, we therefore obtain

$$\beta \sim \frac{U}{L}, \tag{28}$$

where U is the characteristic blood velocity. Thus, for a given capillary length and diameter, β is linearly proportional to blood velocity (or volume flow rate). Considering that capillary flow speeds are typically on the order of 1 mm/s [47], and that $\beta = 10\ \mathrm{s}^{-1}$ yields the best agreement with experimental results, the corresponding length scale is $L \approx 0.1$ mm. This value is much larger than the diffusion length of the system, providing a physical justification for why the intravascular concentration depends primarily on β and not on diffusion across the domain. In reality, capillaries can be as small as a red blood cell in diameter, making intravascular diffusion more complex. Here, however, we lump these complexities into the parameter β, which highlights its importance in this transport problem. To capture a broad range of flow characteristics, including asymptotic behavior, we performed simulations over a wide range of β values.

Figure 3(b) shows the concentration profile for different β values with $N_o/N_i = 1$. A higher value of β corresponds to increased blood velocity and, consequently, stronger clearance from the blood, resulting in lower concentrations in both the inner and outer domains. This relationship is particularly relevant to age-related changes in waste clearance from the brain. Blood velocity decreases with age [48], which may contribute to the elevated levels of Aβ observed in aged brains. The shape of the profile varies for different β values and part of that is due to the different diffusivity between the two domains. For higher β values, the concentration in the vessel decreases, approaching zero. Beyond this point, the vessel concentration can no longer drop further, but increasing β still leads to enhanced clearance, resulting in a smaller concentration difference between the vessel and the brain.

To gain a better understanding of the effects of β and N_o/N_i on the concentration in the blood and brain, we performed simulations across a wider range of these parameters. The averaged steady-state concentrations in the vessel and the brain are shown in Fig. 4 for different receptor number ratios and β values. As seen in Fig. 4(a), increasing the number of receptors on the brain side compared to the blood side leads to a lower average concentration in the brain, as more receptors facilitate the transport of Aβ from the brain to the blood. This behavior is not observed for the concentration in the vessel, where the average concentration remains independent of receptor number ratios [Fig. 4(b)], the same principle we observed in Fig. 3(a).

Figures 4(c) and 4(d) show the variation of concentration in the brain and vessel with β. Since β represents the strength of clearance by advection in the vessel, increasing β results in a decrease in concentration in both domains. However, this dependency is more prominent in the vessel, as the interface boundary acts as a barrier between the concentration in the brain and the sink in the blood.

Another important parameter we analyzed is the vessel size, which can affect the BBB and the concentration of Aβ in the brain. Figures 5(a) and 5(b) show the concentration profiles and the variation of averaged concentration for different vessel diameters, respectively. Here we vary only the vessel diameter while keeping all other parameters constant, including the receptor-to-vessel radius ratio (ϵ) and the total number of receptors. Since there is a sink term in the vessel, an increase in vessel diameter results in a stronger sink effect, leading to lower concentrations in both the vessel and the brain. As the concentration decreases, the level of saturation in the brain tissue also decreases with increasing vessel size. It is important to note that, in our simulations, the domain size (R_b) was fixed while the vessel diameter was varied. This

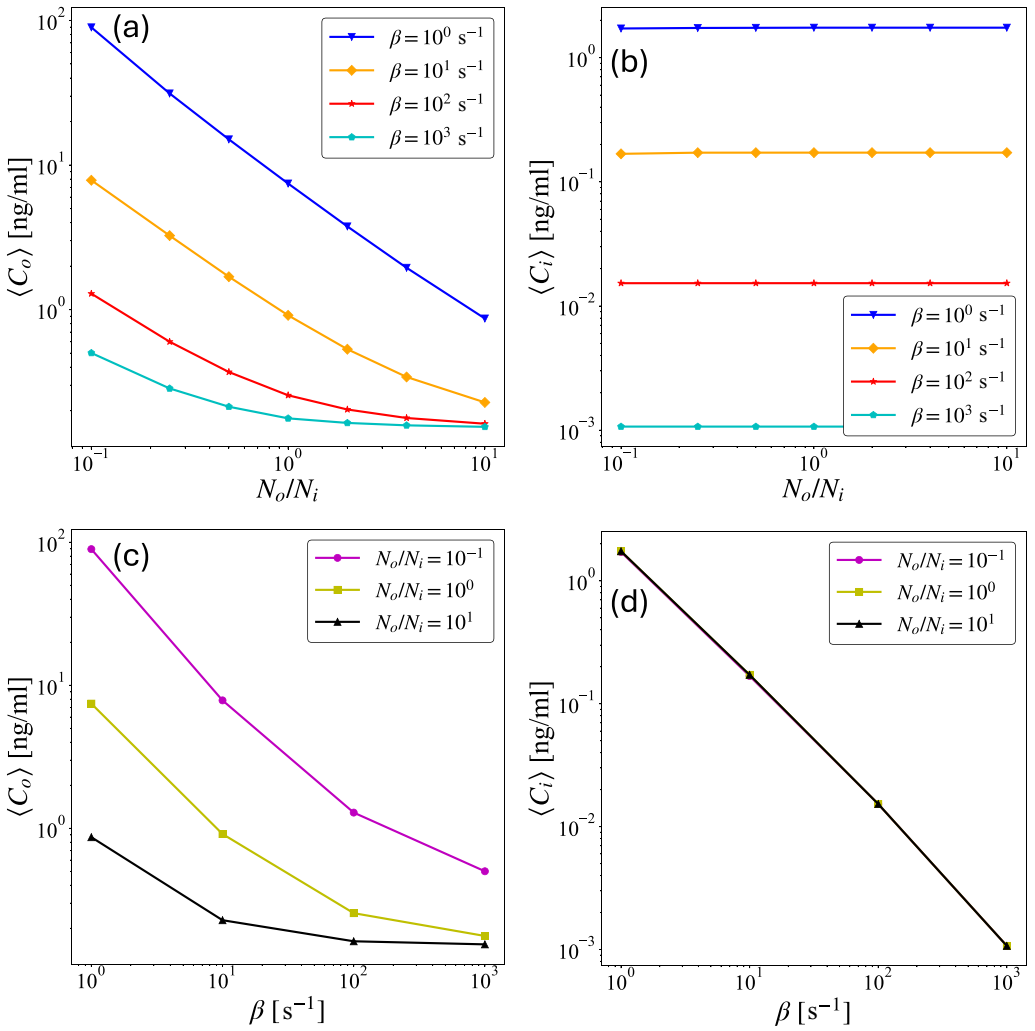

FIG. 4. Spatially averaged steady-state concentrations for different β and N_o/N_i. (a), (b) Average concentration as a function of N_o/N_i for the (a) inner (vessel) or (b) outer (brain) domain. (c), (d) Average concentration as a function of β for the (c) inner (vessel) or (d) outer (brain) domain.

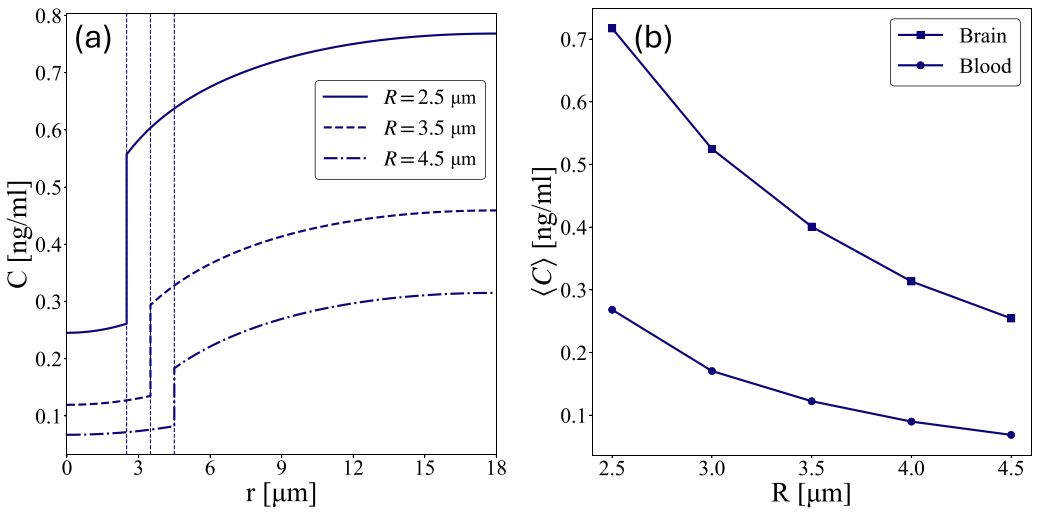

FIG. 5. Steady-state concentration varies with vessel radius. (a) Concentration profiles for three different capillary radii. (b) Spatially averaged concentration for the inner (vessel) and outer (brain) domains as a function of capillary radius.

assumption results in identical vessel density (i.e., number of vessels per unit area) across different vessel diameters. Because larger vessels act as stronger sinks for clearance, this leads to enhanced overall clearance for larger vessel sizes. In reality, however, the density of larger vessels such as arteries and veins is lower than that of smaller vessels such as capillaries. To avoid complexity, this effect was not considered here. A detailed investigation of the interplay between vessel size and vessel density therefore remains an interesting direction for future work.

B. Transient results

So far, we have analyzed the effect of different parameters on the transport rate of Aβ through the BBB in steady state. Although we are solving the diffusion equation, the reaction between Aβ monomers and boundary receptors influences the timescale of transport. In other words, monomers must diffuse through the domain and cross the boundary to be transferred. Here we present results at different time instants to analyze the transient behavior of the system under various brain dynamics. We begin by simulating the transient behavior of Aβ concentration levels in the brain in response to changes in blood flow. First, we perform a steady-state simulation corresponding to the case of $\beta = 1\,\mathrm{s}^{-1}$ and $N_o/N_i = 2$ and use these results as the initial condition. Then, the transient simulation begins by using this initial condition and increasing β to $10\,\mathrm{s}^{-1}$ until reaching a new steady state. Figure 6 shows the concentration profile and the average concentration in the vessel and brain for these transient simulations. Figures 6(a) and 6(b) illustrate the evolution of concentration profiles and averaged concentration respectively, and the time scale of these changes. This analysis demonstrates the effect of increasing blood flow speed on Aβ clearance from the brain. The time required to reach the new steady state when increasing β from 1 to $10\,\mathrm{s}^{-1}$ is approximately 1 min. To calculate the time to steady state, we solve the transient form of the diffusion equation using specified initial conditions and time steps. The final time preceding equilibrium, when a new steady state is reached, is recorded as the time to steady state. A steady state is identified when the criterion $(C^n_{\max} - C^{n-1}_{\max})/C^{n-1}_{\max} < 10^{-10}$ is satisfied.

We next performed the reverse analysis: we take the steady-state results of the case with $\beta = 10\,\mathrm{s}^{-1}$ as the initial condition and begin the transient simulation with β equal to $1\ \mathrm{s}^{-1}$ [Figs. 6(c) and 6(d)]. This analysis characterizes to the effect of reducing blood flow on brain Aβ concentration. An interesting observation here is that the time required to reach steady state is more than five times longer than the previous case. This indicates that increasing blood flow reduces the concentration in the brain much faster than decreasing blood flow increases the concentration. We performed a similar analysis for various 2-, 10-, or 100-fold increases and decreases in β and recorded the time required to reach steady state [Fig. 6(e)]. All the red cases, which represent a *decreased* value of β, consistently take longer to reach steady state compared to the analogous increased β (blue) cases. Additionally, due to the complex nature of the BBB boundary condition, no clear trend can be identified within the blue (increase) or red (decrease) cases when considered separately. These comparisons strongly motivate numerical investigation of phenomena that alter cerebral blood flow and/or capillary diameter, such as sleep and spreading depolarization.

In addition to the β parameter, it is reasonable to question whether other key parameters of our system influence the time required to reach the steady state. In particular, we examined whether this transport is limited by the rate of diffusion or by the reactions occurring at the BBB. Monomers diffuse through space to reach the BBB, where a localized reaction takes place. Therefore, these two processes are inherently coupled, as is also demonstrated in Eq. (15), which includes both diffusion and reaction coefficients. While diffusion time depends directly on the diffusivity, the reaction introduces an additional timescale that contributes to the total time required to reach equilibrium. Consequently, one may expect that for low diffusivities the system is diffusion-limited, whereas for higher diffusivities the reaction time becomes more significant [Supplemental Material Sec. V [40], Fig. S3(a)]. Within the parameter range relevant to our study, the reaction timescale—the difference between the two curves in Fig. S3(a)—is smaller than that of diffusion timescale. To examine this behavior more closely, we plot $C_\alpha/(K_\alpha + C_\alpha)$ (which is the fraction of V_α achieved) over time for the case illustrated in Fig. 6(a) [Supplemental Material Sec. V [40], Fig. S3(b)]. This fraction remains well below 0.5 during the transition between steady states, indicating that additional transporters remain available and the BBB is undersaturated. Therefore, under the conditions of our model, diffusion is more limiting than the reaction at the boundary.

To analyze the dynamics of Aβ concentration in the brain and blood during sleep, we simulated a sleep cycle for mice. We assumed a cycle consisting of 8 min of non-REM (NREM) sleep and 1 min of rapid eye movement (REM) sleep [49]. While it has been shown that arterial diameter changes during different sleep phases [50], the size of capillaries remains constant. However, the velocity of blood flow during REM is approximately twice as high as during NREM and awake states [51]. We simulated a transient scenario for REM and NREM phases using $N_o/N_i = 2$ and varied β between $10\,\mathrm{s}^{-1}$ and $20\,\mathrm{s}^{-1}$. The results are shown in Fig. 7. In each REM cycle, the average concentration of Aβ in the blood vessel and the brain decreases by 51% and 34%, respectively, and equilibrium at that lower concentration is reached after about half the REM duration. This suggests that REM sleep may, in addition to a myriad of other vital functions [52], aid the brain in removing Aβ. Note that the difference in transient time (required to reach steady state) in this case is substantially less than that of Figs. 6(c) and 6(d) because the change in β is smaller.

Finally, we simulated transient effects due to a pathological phenomenon known as "spreading depolarization" (SD). As mentioned above, SD occurs due to loss of brain ion homeostasis that propagates as a wave through the cerebral cortex [34]. During this process, the size of the brain vasculature varies over time, with capillaries experiencing three sequential phases. Phase I lasts for 1 min and involves vasoconstriction, with an average decrease of 8.2% in capillary radius compared to baseline (this average is taken across first-, second-, and third-order capillaries). Phase II follows Phase I and lasts for about 3 min, during which the capillary radius increases by

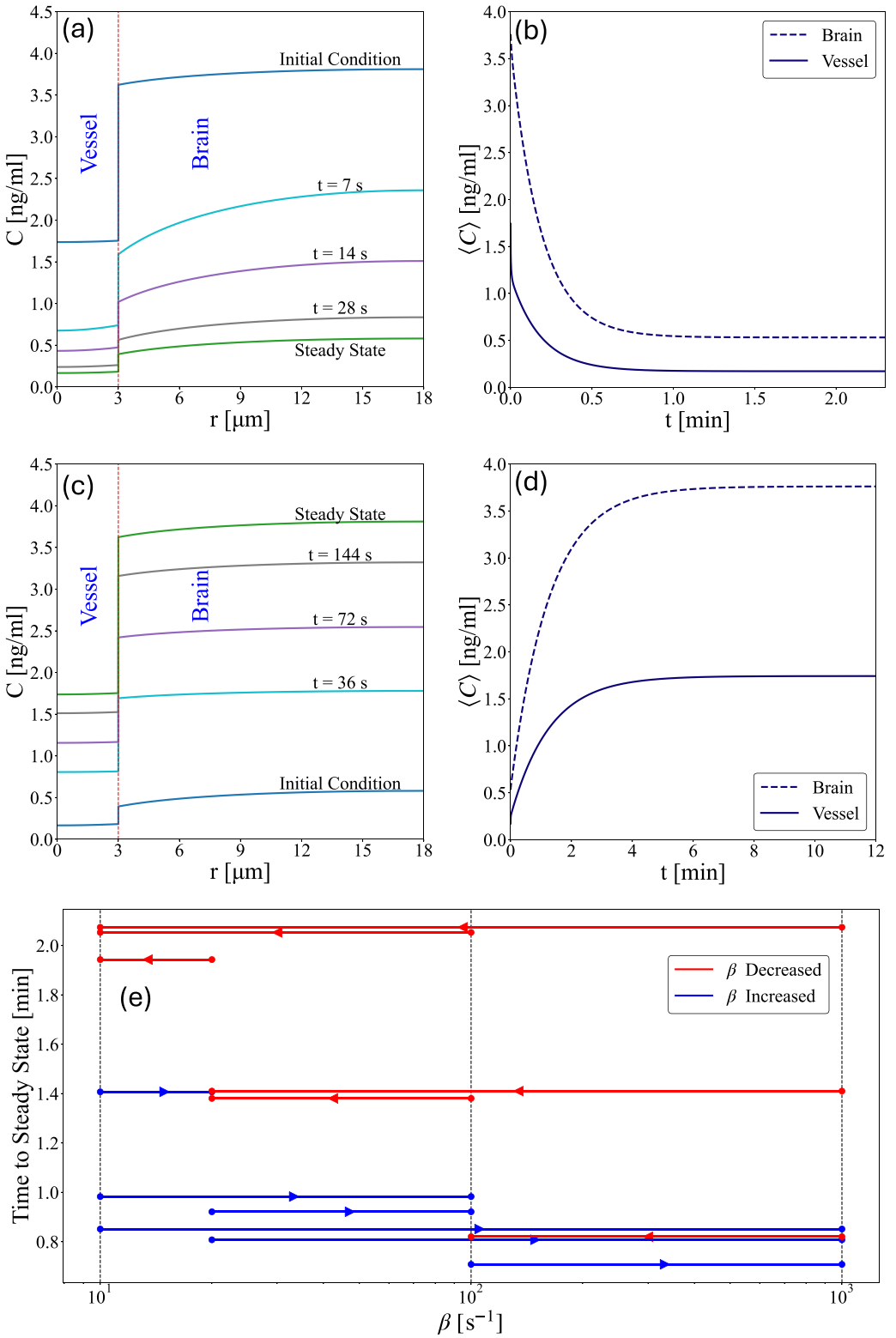

FIG. 6. Transient times are shorter for increasing β than decreasing β. (a) Transient variation of the concentration profile and (b) spatially averaged concentration when β is increased from 1 to 10 s^{-1}. (c) Transient variation of the concentration profile and (d) spatially averaged concentration when β is decreased from 10 to 1 s^{-1}. (e) Time needed to reach steady state for different increases and decreases of β. All plots correspond to $N_o/N_i = 2$.

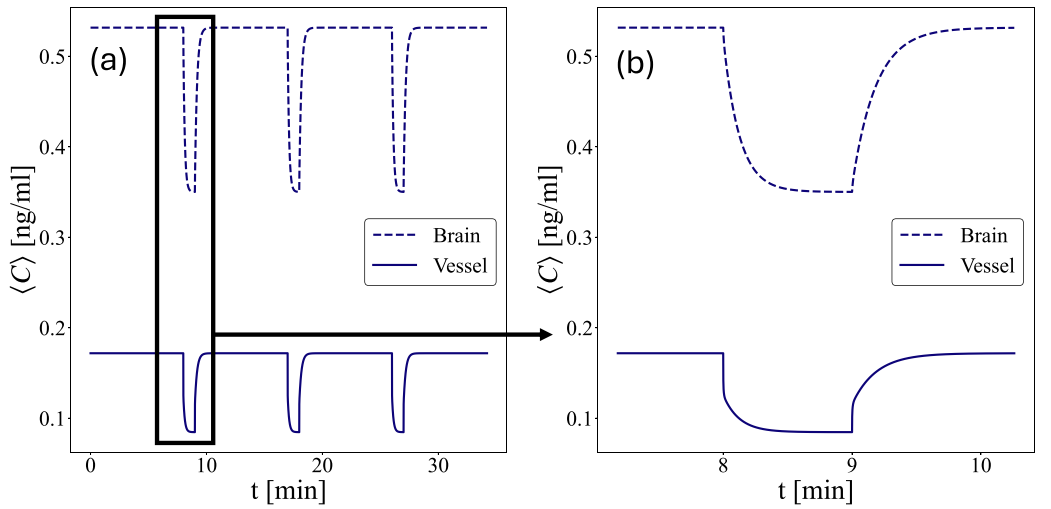

FIG. 7. Aβ concentration during sleep suggests REM sleep may play an important role in waste clearance. (a) Three sleep cycles consisting of 8 min of NREM sleep and 1 min of REM sleep. (b) A zoomed-in enlargment of the 2.5-min period indicated in (a). In all cases, β changes between 10 and 20 s^{-1} in NREM and REM sleep, respectively.

an average of 12.5% relative to baseline. Finally, in Phase III, a persistent vasoconstriction occurs, reducing the capillary radius by 11.2% compared to baseline [53]. We performed a time-varying simulation of this process using default values of $\beta = 10\,s^{-1}$, $N_o/N_i = 1$, and a baseline capillary radius of 3 μm. As shown in Fig. 8, the concentration of Aβ varies in response to changes in capillary size, and the different timescales of these phases lead to a reduced then increased steady-state Aβ concentration during Phases II and III, respectively. In the latter case, Aβ is elevated by 28% and 22% (compared to the baseline concentration before SD) in the vessel and brain tissue, respectively. These transient simulations demonstrate the capability of the derived BBB boundary condition to model different brain states and the dynamic behavior of brain vasculature.

IV. CONCLUSION

In this study, we introduced a mathematical model to describe the blood-brain barrier (BBB), incorporating receptor kinetics and accounting for both the number and properties of active transporters on either side of the BBB. Starting from a finite receptor kinetics model, we extended boundary homogenization to derive an effective boundary condition for solute flux between two domains representing the brain and the blood. This boundary condition accounts for bidirectional transport between the two domains ensuring mass conservation, and it incorporates nonlinear receptor-mediated kinetics, enabling the first mathematical representation of BBB transport processes. We used this boundary model to simulate Aβ transport between the brain and blood, largely motivated

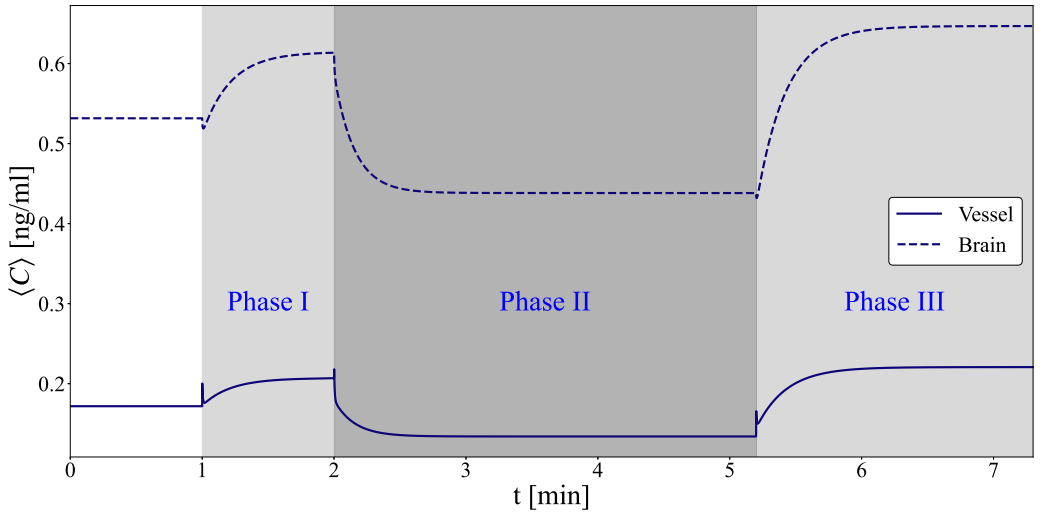

FIG. 8. Averaged Aβ concentration variation in the brain and vessel for different phases of spreading depolarization for mice brain. Phase I: 60 s, 8.2% decrease in capillary radius relative to baseline; Phase II: 3 min, 12.5% increase in capillary radius relative to baseline; Phase III: persistent, 11.2% decrease in capillary radius relative to baseline. Note that the brief jumps or drops in the concentrations at the beginning of each phase are small numerical artifacts that arise due to the concentration profile adjusting following sudden changes in the size of the vessel/brain domain.

by the important role that impaired Aβ clearance plays in pathogenesis of Alzheimer's disease and related dementias [2,54]. We applied the derived boundary condition to an axisymmetric cylindrical geometry, representing a capillary surrounded by brain tissue, and incorporated relevant biophysical parameters such as receptor density, diffusivity, and Aβ production rates. The governing equations were nondimensionalized (Supplemental Material Sec. I [40]) and solved numerically using a finite difference method. Both steady-state and transient simulations were performed to investigate the influence of key parameters such as receptor number ratio, blood clearance rate, and vessel diameter on Aβ distribution. Our numerical results were verified against the steady-state analytical solution (Supplemental Material Sec. IV [40]) and then leveraged to characterize parametric dependencies.

Our results show that the receptor number ratio N_o/N_i significantly affects Aβ concentration in the brain but not in the blood, consistent with the analytical solution. This sensitivity to receptor number ratio may, in part, explain why aging is the greatest risk factor for Alzheimer's disease [55]. An earlier study reported that LRP1 expression *decreases* up to 6.4-fold and RAGE *increases* up to 82-fold with aging (in mice) [56]. Hence, N_o/N_i decreases by over two orders of magnitude across the murine lifespan, suggesting that the brain Aβ equilibrium concentration could increase 10-fold or more [Fig. 4(c)] due to this factor alone.

The blood clearance rate β was also found to play a very significant role in regulating Aβ levels in both compartments, with increasing β lowering concentrations more rapidly in the vessel than in the brain. Specifically, increasing β by a factor of 1000 decreased blood and brain Aβ concentration by about three orders of magnitude and up to about two orders of magnitude, respectively [Figs. 4(c) and 4(d)]. Notably, the change in Aβ concentration in the blood is independent of N_o/N_i, but the *rate of change* in brain concentration with the respect to β is greater when N_o/N_i is smaller, as occurs with aging [compare purple and black curves in Fig. 4(c)]. This leads to an interesting observation with important therapeutic implications: although aging-related decrease in N_o/N_i likely leads to larger Aβ concentrations in brain tissue, our model suggests there is an increasing sensitivity to elevated blood flow in this regime. Hence, approaches for elevating cerebral blood flow, such as exercise [57] or neuromodulation [58], may be especially important for reducing Aβ load in old age. A related prediction from our model involves the temporal asymmetry that arises in transient simulations: increasing blood flow led to faster reduction in brain Aβ than the rate of Aβ increase observed when blood flow was reduced (Fig. 6). Hence, even brief increases in cerebral blood flow (such as during REM sleep) may have a disproportionately large effect on Aβ clearance. Our model also predicts that reductions in blood flow (i.e., decreased β) in aging (i.e., when N_o/N_i decreases) will lead to substantial increases in brain Aβ concentrations. There is evidence suggesting this effect contributes to pathogenesis of cognitive impairment and dementia, although causality has been difficult to establish in experiments [48].

We demonstrated our model's applicability to complex physiology by simulating sleep as a cycle of variations in blood flow (captured by varying β). Based on a twofold change in blood flow, motivated by published experimental measurements [51], our model predicts that the Aβ concentration in the blood and brain each decrease by 50% and 34% (during the REM phase, compared to NREM), respectively. An important, open question concerns the evolutionary necessity of two-phase (NREM and REM) sleep across most animal species [59]. Our results (Fig. 7) suggest that REM sleep may play an important role in enhancing Aβ clearance. Indeed, the timescale for murine REM sleep (about 1 min) is only a bit longer than the time required to reach equilibrium at the lower Aβ concentration. This can be further rationalized by considering another waste clearance pathway in the brain, the glymphatic system, which is most active during NREM sleep [60]. The glymphatic system is an important pathway for solute exchange between cerebrospinal fluid (CSF) and interstitial fluid [3]. We have recently shown that Aβ clearance depends on both BBB and glymphatic function, and that overall clearance is synergistically amplified when both clearance mechanisms are present [42]. Hence, the glymphatic system may transport interstitial Aβ to the vicinity of blood vessels during NREM sleep and BBB efflux—combined with elevated blood flow—may enhance Aβ clearance during REM sleep. In future experimental and numerical studies, we intend to test this hypothesis about how the structure of a sleep cycle may maximize brain Aβ clearance.

We also simulated a complex pathological phenomenon, spreading depolarization (SD). SD refers to the loss of brain ion homeostasis, which propagates through the cortex as a reaction-diffusion wave and is associated with migraine with aura, stroke, traumatic brain injury, and more [34]. SD elicits changes in capillary diameter, likely due to SD-related calcium ionic signaling to pericytes (cells that wrap around capillaries) [53]. Our model suggests that changes in capillary diameter alone can lead to large disruptions in brain Aβ concentration (Fig. 8), with decreases as much as 18% for more than 2 min (Phase II) and increases by up to 22% for over 1 min (Phase III). This highlights the prospect of ionic manipulation of pericytes to augment brain microcirculation [61], potentially increasing Aβ clearance. A limitation of our approach is that we only modeled the variation in vessel diameter and not the associated complex changes in blood flow, including flow stagnation, which has been reported in prior studies [62,63]. When this additional factor is accounted for, the maximum increase in brain Aβ is likely to be significantly higher that our simulations predict. These elevated Aβ concentrations may help explain why migraine has been associated with an increased risk of dementia [36,37].

The trends in Aβ concentration reported in this article are compatible with existing preclinical and clinical understanding, but limited data are available for quantitatively verifying these predictions. Cerebral blood flow is known to decrease with aging [48], and growing evidence suggests that this decrease precedes cognitive impairment and thus may directly contribute to disease pathology [64,65]. Brain regions with higher Aβ load have also been linked to local reduction in cerebral blood flow [66]. Sleep deprivation has also been shown to acutely increase Aβ concentration in both mice [67,68] and humans [69]. However, spatially and/or temporally resolved *in vivo* measurements of Aβ are scarce [70–72], and none have characterized variation of Aβ concentration in the vicinity of a capillary to the best of our knowledge.

Future experiments may leverage *in vivo* microdialysis [73] or microimmunoelectrode measurements [70] to probe Aβ concentration at a particular location in the brain with temporal resolution as high as $1\,\mathrm{min}^{-1}$. Other emerging technologies, such as *in vivo* imaging with fluorescent compounds that bind to Aβ [71,72], could also yield measurements for quantitatively testing our predictions and facilitating future work aimed at developing more realistic and sophisticated numerical models of BBB transport.

There are several notable limitations of this study. Our model geometry is highly idealized, consisting of a 1D (i.e., axisymmetric two-dimensional) domain. While this assumption facilitates ease of data interpretation and computational tractability, true brain vasculature is much more heterogeneous and complex, which certainly alters Aβ concentrations. Our simplified geometry also employs a blood sink term ($-\beta C_i$) rather than solving the much more complex problem of (non-Newtonian) blood flow in a capillary. In addition, our model considers only one type of vessel: a capillary immediately surrounded by brain tissue. Larger vessels, including arteries and veins, are immediately surrounded by a perivascular space filled with flowing CSF [74]. Hence, Aβ clearance in the vicinity of these larger vessels likely involves interactions between the glymphatic system and BBB [42], rendering such simulations substantially more complex. We note that there is some evidence that capillaries may have a perivascular space [8], which we have neglected in this study. Lastly, our modeling of sleep and SD are highly idealized with several assumptions, including a constant rate of Aβ generation (G). A very recent study in humans indicates that metabolism decreases during NREM sleep, suggesting Aβ production may also decrease [75]. Future studies should improve upon these numerous limitations and may even eventually perform mouse-specific simulations of geometry and vascular dynamics obtained *in vivo* using high-resolution optical imaging techniques such as two-photon microscopy.

Overall, this work introduces a mechanistic and biophysically grounded boundary condition for solute exchange via active transporters at the BBB, offering a valuable tool for future studies on drug delivery, brain waste clearance, and modeling pathogenesis of neurodegenerative diseases. Future simulations could probe active transport of molecules other than Aβ, including glucose, lactate, amino acids, or pharmaceuticals [4,76]. Such simulations may generate predictions that guide future experiments. The considerable dependence on receptor number ratio and β suggest future experiments should seek to better quantify these important parameters. However, β arises as an idealization of blood flow, so future modeling studies could instead focus on extending our idealized axisymmetric model to more realistic two- or three-dimensional domains with explicit implementation of blood flow to improve understanding of BBB active transport.

ACKNOWLEDGMENTS

Research reported in this publication was supported by the National Institute of Biomedical Imaging and Bioengineering of the National Institutes of Health under Award No. R21EB036217. The content is solely the responsibility of the authors and does not necessarily represent the official views of the National Institutes of Health. This work was also supported by the Burroughs Wellcome Fund's Career Award at the Scientific Interface to G.H.

DATA AVAILABILITY

The data that support the findings of this article are openly available [77].

[1] C. R. Jack, D. S. Knopman, W. J. Jagust, L. M. Shaw, P. S. Aisen, M. W. Weiner, R. C. Petersen, and J. Q. Trojanowski, Hypothetical model of dynamic biomarkers of the Alzheimer's pathological cascade, Lancet Neurol. **9**, 119 (2010).

[2] K. G. Mawuenyega, W. Sigurdson, V. Ovod, L. Munsell, T. Kasten, J. C. Morris, K. E. Yarasheski, and R. J. Bateman, Decreased clearance of CNS β-amyloid in Alzheimer's disease, Science **330**, 1774 (2010).

[3] M. Nedergaard and S. A. Goldman, Glymphatic failure as a final common pathway to dementia, Science **370**, 50 (2020).

[4] S. B. Hladky and M. A. Barrand, Elimination of substances from the brain parenchyma: Efflux via perivascular pathways and via the blood–brain barrier, Fluids Barriers CNS **15**, 30 (2018).

[5] K. F. Roberts, D. L. Elbert, T. P. Kasten, B. W. Patterson, W. C. Sigurdson, R. E. Connors, V. Ovod, L. Y. Munsell, K. G. Mawuenyega, M. M. Miller-Thomas *et al.*, Amyloid-β efflux from the central nervous system into the plasma, Ann. Neurol. **76**, 837 (2014).

[6] J. J. Iliff, M. Wang, Y. Liao, B. A. Plogg, W. Peng, G. A. Gundersen, H. Benveniste, G. E. Vates, R. Deane, S. A. Goldman *et al.*, A paravascular pathway facilitates CSF flow through the brain parenchyma and the clearance of interstitial solutes, including amyloid β, Sci. Transl. Med. **4**, 147ra111 (2012).

[7] D. H. Kelley, Brain cerebrospinal fluid flow, Phys. Rev. Fluids **6**, 070501 (2021).

[8] M.-J. Hannocks, M. E. Pizzo, J. Huppert, T. Deshpande, N. J. Abbott, R. G. Thorne, and L. Sorokin, Molecular characterization of perivascular drainage pathways in the murine brain, J. Cerebr. Blood Flow Met. **38**, 669 (2018).

[9] M. X. Wang, L. Ray, K. F. Tanaka, J. J. Iliff, and J. Heys, Varying perivascular astroglial endfoot dimensions along the vascular tree maintain perivascular-interstitial flux through the cortical mantle, Glia **69**, 715 (2021).

[10] S. E. Storck, S. Meister, J. Nahrath, J. N. Meißner, N. Schubert, A. Di Spiezio, S. Baches, R. E. Vandenbroucke, Y. Bouter, I. Prikulis *et al.*, Endothelial LRP1 transports amyloid-β_{1-42} across the blood-brain barrier, J. Clin. Invest. **126**, 123 (2016).

[11] H. Qosa, B. S. Abuasal, I. A. Romero, B. Weksler, P.-O. Couraud, J. N. Keller, and A. Kaddoumi, Differences in amyloid-β clearance across mouse and human blood–brain

barrier models: Kinetic analysis and mechanistic modeling, Neuropharmacology **79**, 668 (2014).
[12] R. Daneman and A. Prat, The blood–brain barrier, CSH Perspect. Biol. **7**, a020412 (2015).
[13] I. Y. Petrushanko, V. A. Mitkevich, and A. A. Makarov, Effect of β-amyloid on blood-brain barrier properties and function, Biophys. Rev. **15**, 183 (2023).
[14] J. R. Cirrito, R. Deane, A. M. Fagan, M. L. Spinner, M. Parsadanian, M. B. Finn, H. Jiang, J. L. Prior, A. Sagare, K. R. Bales *et al.*, P-glycoprotein deficiency at the blood-brain barrier increases amyloid-β deposition in an Alzheimer disease mouse model, J. Clin. Invest. **115**, 3285 (2005).
[15] B. V. Zlokovic, R. Deane, A. P. Sagare, R. D. Bell, and E. A. Winkler, Low-density lipoprotein receptor-related protein-1: A serial clearance homeostatic mechanism controlling Alzheimer's amyloid β-peptide elimination from the brain, J. Neurochem. **115**, 1077 (2010).
[16] R. Deane, R. D. Bell, A. Sagare, and B. V. Zlokovic, Clearance of amyloid-β peptide across the blood-brain barrier: Implication for therapies in Alzheimer's disease, CNS Neurol. Disord. Drug Targets **8**, 16 (2009).
[17] R. Deane, S. Du Yan, R. K. Submamaryan, B. LaRue, S. Jovanovic, E. Hogg, D. Welch, L. Manness, C. Lin, J. Yu *et al.*, RAGE mediates amyloid-β peptide transport across the blood-brain barrier and accumulation in brain, Nat. Med. **9**, 907 (2003).
[18] R. Deane, I. Singh, A. P. Sagare, R. D. Bell, N. T. Ross, B. LaRue, R. Love, S. Perry, N. Paquette, R. J. Deane *et al.*, A multimodal rage-specific inhibitor reduces amyloid β–mediated brain disorder in a mouse model of Alzheimer disease, J. Clin. Invest. **122**, 1377 (2012).
[19] W. Zhang, H. Xiong, D. Callaghan, H. Liu, A. Jones, K. Pei, D. Fatehi, E. Brunette, and D. Stanimirovic, Blood-brain barrier transport of amyloid beta peptides in efflux pump knock-out animals evaluated by in vivo optical imaging, Fluids Barriers CNS **10**, 13 (2013).
[20] J. E. Donahue, S. L. Flaherty, C. E. Johanson, J. A. Duncan, G. D. Silverberg, M. C. Miller, R. Tavares, W. Yang, Q. Wu, E. Sabo *et al.*, RAGE, LRP-1, and amyloid-beta protein in Alzheimer's disease, Acta Neuropathol. **112**, 405 (2006).
[21] H. C. Berg and E. M. Purcell, Physics of chemoreception, Biophys. J. **20**, 193 (1977).
[22] R. Zwanzig and A. Szabo, Time dependent rate of diffusion-influenced ligand binding to receptors on cell surfaces, Biophys. J. **60**, 671 (1991).
[23] A. Cornish-Bowden, One hundred years of Michaelis–Menten kinetics, Perspect. Sci. **4**, 3 (2015).
[24] G. Handy, S. D. Lawley, and A. Borisyuk, Role of trap recharge time on the statistics of captured particles, Phys. Rev. E **99**, 022420 (2019).
[25] D. Shoup and A. Szabo, Role of diffusion in Ligand binding to macromolecules and cell-bound receptors, Biophys. J. **40**, 33 (1982).
[26] F. C. Collins and G. E. Kimball, Diffusion-controlled reaction rates, J. Colloid Sci. **4**, 425 (1949).
[27] A. E. Lindsay, A. J. Bernoff, and M. J. Ward, First passage statistics for the capture of a Brownian particle by a structured spherical target with multiple surface traps, Multiscale Model. Simul. **15**, 74 (2017).
[28] A. J. Bernoff, A. E. Lindsay, and D. D. Schmidt, Boundary homogenization and capture time distributions of semipermeable membranes with periodic patterns of reactive sites, Multiscale Model. Simul. **16**, 1411 (2018).
[29] C. E. Plunkett and S. D. Lawley, Bimolecular binding rates for pairs of spherical molecules with small binding sites, Multiscale Model. Simul. **19**, 148 (2021).
[30] G. Handy and S. D. Lawley, Revising Berg-Purcell for finite receptor kinetics, Biophys. J. **120**, 2237 (2021).
[31] Y.-E. S. Ju, S. J. Ooms, C. Sutphen, S. L. Macauley, M. A. Zangrilli, G. Jerome, A. M. Fagan, E. Mignot, J. M. Zempel, J. A. H. R. Claassen, and D. M. Holtzman, Slow wave sleep disruption increases cerebrospinal fluid amyloid-β levels, Brain **140**, 2104 (2017).
[32] B. P. Lucey and R. J. Bateman, Amyloid-β diurnal pattern: Possible role of sleep in Alzheimer's disease pathogenesis, Neurobiol. Aging **35**, S29 (2014).
[33] L. Rigat, K. Ouk, A. Kramer, and J. Priller, Dysfunction of circadian and sleep rhythms in the early stages of Alzheimer's disease, Acta Physiologica **238**, e13970 (2023).
[34] J. P. Dreier, The role of spreading depression, spreading depolarization and spreading ischemia in neurological disease, Nat. Med. **17**, 439 (2011).
[35] D. R. Kramer, T. Fujii, I. Ohiorhenuan, and C. Y. Liu, Cortical spreading depolarization: Pathophysiology, implications, and future directions, J. Clin. Neurosci. **24**, 22 (2016).
[36] C.-S. Chuang, C.-L. Lin, M.-C. Lin, F.-C. Sung, and C.-H. Kao, Migraine and risk of dementia: A nationwide retrospective cohort study, Neuroepidemiology **41**, 139 (2013).
[37] S.-Y. Lee, J.-S. Lim, D. J. Oh, I. G. Kong, and H. G. Choi, Increased risk of neurodegenerative dementia in women with migraines: A nested case–control study using a national sample cohort, Medicine **98**, e14467 (2019).
[38] J. Gunawardena, Distributivity and processivity in multisite phosphorylation can be distinguished through steady-state invariants, Biophys. J. **93**, 3828 (2007).
[39] G. E. Briggs and J. B. S. Haldane, A note on the kinetics of enzyme action, Biochem. J. **19**, 338 (1925).
[40] See Supplemental Material at http://link.aps.org/supplemental/10.1103/qr7v-btpp for equation nondimensionalization, comparison with a linear boundary condition, details of numerical methods, an analytical solution, and discussion of transport timescales.
[41] E. Syková and C. Nicholson, Diffusion in brain extracellular space, Physiol. Rev. **88**, 1277 (2008).
[42] R. Yousofvand and J. Tithof, Numerical simulations reveal complementary function of blood-brain barrier and glymphatic transport in the brain, Phys. Rev. Lett. **134**, 138403 (2025).
[43] X. Ji, T. Ferreira, B. Friedman, R. Liu, H. Liechty, E. Bas, J. Chandrashekar, and D. Kleinfeld, Brain microvasculature has a common topology with local differences in geometry that match metabolic load, Neuron **109**, 1168 (2021).
[44] C. R. Kyrtsos and J. S. Baras, Modeling the role of the glymphatic pathway and cerebral blood vessel properties in Alzheimer's disease pathogenesis, PLoS ONE **10**, e0139574 (2015).
[45] T. Miyawaki, S. Morikawa, E. A. Susaki, A. Nakashima, H. Takeuchi, S. Yamaguchi, H. R. Ueda, and Y. Ikegaya, Visualization and molecular characterization of whole-brain vascular

networks with capillary resolution, Nat. Commun. **11**, 1104 (2020).
[46] S. M. Cho, S. Lee, S.-H. Yang, H. Y. Kim, M. J. Lee, H. V. Kim, J. Kim, S. Baek, J. Yun, D. Kim *et al.*, Age-dependent inverse correlations in CSF and plasma amyloid-β(1–42) concentrations prior to amyloid plaque deposition in the brain of 3xTg-AD mice, Sci. Rep. **6**, 20185 (2016).
[47] G. Meng, J. Zhong, Q. Zhang, J. S. J. Wong, J. Wu, K. K. Tsia, and Na Ji, Ultrafast two-photon fluorescence imaging of cerebral blood circulation in the mouse brain in vivo, Proc. Natl. Acad. Sci. USA **119**, e2117346119 (2022).
[48] N. Mokhber, A. Shariatzadeh, A. Avan, H. Saber, G. S. Babaei, G. Chaimowitz, and M. R. Azarpazhooh, Cerebral blood flow changes during aging process and in cognitive disorders: A review, Neuroradiol. J. **34**, 300 (2021).
[49] S.-H. Park, J. Baik, J. Hong, H. Antila, B. Kurland, S. Chung, and F. Weber, A probabilistic model for the ultradian timing of REM sleep in mice, PLoS Comput. Biol. **17**, e1009316 (2021).
[50] L. Bojarskaite, A. Vallet, D. M. Bjørnstad, K. M. Gullestad Binder, C. Cunen, K. Heuser, M. Kuchta, K.-A. Mardal, and R. Enger, Sleep cycle-dependent vascular dynamics in male mice and the predicted effects on perivascular cerebrospinal fluid flow and solute transport, Nat. Commun. **14**, 953 (2023).
[51] C. J. Tsai, T. Nagata, C. Y. Liu, T. Suganuma, T. Kanda, T. Miyazaki, K. Liu, T. Saitoh, H. Nagase, M. Lazarus *et al.*, Cerebral capillary blood flow upsurge during REM sleep is mediated by A2a receptors, Cell Rep. **36**, 109558 (2021).
[52] Y. Mukai and A. Yamanaka, Functional roles of REM sleep, Neurosci. Res. **189**, 44 (2023).
[53] L. Khennouf, B. Gesslein, A. Brazhe, J. C. Octeau, N. Kutuzov, B. S. Khakh, and M. Lauritzen, Active role of capillary pericytes during stimulation-induced activity and spreading depolarization, Brain **141**, 2032 (2018).
[54] H. Hampel, J. Hardy, K. Blennow, C. Chen, G. Perry, S. H. Kim, V. L. Villemagne, P. Aisen, M. Vendruscolo, T. Iwatsubo *et al.*, The amyloid-β pathway in Alzheimer's disease, Mol. Psychiatry **26**, 5481 (2021).
[55] R. Guerreiro and J. Bras, The age factor in Alzheimer's disease, Genome Med. **7**, 106 (2015).
[56] D. Osgood, M. C. Miller, A. A. Messier, L. Gonzalez, and G. D. Silverberg, Aging alters mRNA expression of amyloid transporter genes at the blood-brain barrier, Neurobiol. Aging **57**, 178 (2017).
[57] L. Mulser and D. Moreau, Effect of acute cardiovascular exercise on cerebral blood flow: A systematic review, Brain Res. **1809**, 148355 (2023).
[58] T. G. White, K. Powell, K. A. Shah, H. H. Woo, R. K. Narayan, and C. Li, Trigeminal nerve control of cerebral blood flow: A brief review, Front. Neurosci. **15**, 649910 (2021).
[59] O. Le Bon, Relationships between REM and NREM in the NREM-REM sleep cycle: A review on competing concepts, Sleep Med. **70**, 6 (2020).
[60] L. Xie, H. Kang, Q. Xu, M. J. Chen, Y. Liao, M. Thiyagarajan, J. O' Donnell, D. J. Christensen, C. Nicholson, J. J. Iliff *et al.*, Sleep drives metabolite clearance from the adult brain, Science **342**, 373 (2013).
[61] T. A. Longden, D. C. Hill-Eubanks, and M. T. Nelson, Ion channel networks in the control of cerebral blood flow, J. Cerebr. Blood F. Metab. **36**, 492 (2016).
[62] J. Chuquet, L. Hollender, and E. A. Nimchinsky, High-resolution in vivo imaging of the neurovascular unit during spreading depression, J. Neurosci. **27**, 4036 (2007).
[63] M. Unekawa, Y. Tomita, H. Toriumi, T. Osada, K. Masamoto, H. Kawaguchi, Y. Itoh, I. Kanno, and N. Suzuki, Hyperperfusion counteracted by transient rapid vasoconstriction followed by long-lasting oligemia induced by cortical spreading depression in anesthetized mice, J. Cereb. Blood Flow Metab. **35**, 689 (2015).
[64] M. Wirth, A. Pichet Binette, P. Brunecker, T. Köbe, A. V. Witte, and A. Flöel, Divergent regional patterns of cerebral hypoperfusion and gray matter atrophy in mild cognitive impairment patients, J. Cereb. Blood Flow Metab. **37**, 814 (2017).
[65] J. F. Leijenaar, I. S. van Maurik, J. P. A. Kuijer, W. M. van der Flier, P. Scheltens, F. Barkhof, and N. D. Prins, Lower cerebral blood flow in subjects with Alzheimer's dementia, mild cognitive impairment, and subjective cognitive decline using two-dimensional phase-contrast magnetic resonance imaging, Alzheimers Dement (Amst) **9**, 76 (2017).
[66] N. Mattsson, D. Tosun, P. S. Insel, A. Simonson, C. R. Jack, L. A. Beckett, M. Donohue, W. Jagust, N. Schuff, and M. W. Weiner, Association of brain amyloid-β with cerebral perfusion and structure in Alzheimer's disease and mild cognitive impairment, Brain **137**, 1550 (2014).
[67] J.-E. Kang, M. M. Lim, R. J. Bateman, J. J. Lee, L. P. Smyth, J. R. Cirrito, N. Fujiki, S. Nishino, and D. M. Holtzman, Amyloid-β dynamics are regulated by orexin and the sleep-wake cycle, Science **326**, 1005 (2009).
[68] N. Cankar, N. Beschorner, A. Tsopanidou, F. L. Qvist, A. R. Colaço, M. Andersen, C. Kjaerby, C. Delle, M. Lambert, F. Mundt *et al.*, Sleep deprivation leads to non-adaptive alterations in sleep microarchitecture and amyloid-β accumulation in a murine Alzheimer model, Cell Rep. **43**, 114977 (2024).
[69] E. Shokri-Kojori, G.-J. Wang, C. E. Wiers, S. B. Demiral, M. Guo, S. W. Kim, E. Lindgren, V. Ramirez, A. Zehra, C. Freeman *et al.*, β-amyloid accumulation in the human brain after one night of sleep deprivation, Proc. Natl. Acad. Sci. USA **115**, 4483 (2018).
[70] C. M. Yuede, H. Lee, J. L. Restivo, T. A. Davis, J. C. Hettinger, C. E. Wallace, K. L. Young, M. R. Hayne, G. Bu, C.-z. Li *et al.*, Rapid in vivo measurement of β-amyloid reveals biphasic clearance kinetics in an Alzheimer's mouse model, J. Exp. Med. **213**, 677 (2016).
[71] R. Tao, N. Wang, T. Shen, Y. Tan, Y. Ren, W. Wei, M. Liao, D. Tan, C. Tang, N. Xu *et al.*, High-fidelity imaging of amyloid-beta deposits with an ultrasensitive fluorescent probe facilitates the early diagnosis and treatment of Alzheimer's disease, Theranostics **12**, 2549 (2022).
[72] N. Byron, N. McAlinden, F. Pisano, M. Pisanello, J. Ferreira, C. Montinaro, K. Mathieson, M. De Vittorio, F. Pisanello, and S. Sakata, Depth-resolved fiber photometry of amyloid plaque signals in freely behaving Alzheimer's disease mice, Neurophotonics **12**, 035014 (2025).
[73] J. R. Cirrito, P. C. May, M. A. O'Dell, J. W. Taylor, M. Parsadanian, J. W. Cramer, J. E. Audia, J. S. Nissen, K. R. Bales, S. M. Paul *et al.*, In vivo assessment of brain interstitial fluid with microdialysis reveals plaque-associated changes in amyloid-β metabolism and half-life, J. Neurosci. **23**, 8844 (2003).

[74] J. M. Wardlaw, H. Benveniste, M. Nedergaard, B. V. Zlokovic, H. Mestre, H. Lee, F. N. Doubal, R. Brown, J. Ramirez, B. J. MacIntosh *et al.*, Perivascular spaces in the brain: Anatomy, physiology and pathology, Nat. Rev. Neurol. **16**, 137 (2020).

[75] J. E. Chen, L. D. Lewis, S. E. Coursey, C. Catana, J. R. Polimeni, J. Fan, K. S. Droppa, R. Patel, H.-Y. Wey, C. Chang *et al.*, Simultaneous EEG-PET-MRI identifies temporally coupled and spatially structured brain dynamics across wakefulness and NREM sleep, Nat. Commun. **16**, 8887 (2025).

[76] D. Wu, Q. Chen, X. Chen, F. Han, Z. Chen, and Y. Wang, The blood–brain barrier: Structure, regulation and drug delivery, Signal Transduct. Target. Ther. **8**, 217 (2023).

[77] The code to reproduce the main figures of this paper, along with demos for running the simulations, is available in a publicly accessible zenodo repository: https://doi.org/10.5281/zenodo.17498471.